RSC Applied Polymers

ROYAL SOCIETY OF CHEMISTRY

PAPER

View Article Online
View Journal | View Issue

Cite this: *RSC Appl. Polym.*, 2025, **3**, 391

Immobilization and electroactive switching of bovine serum albumin on polypyrrole functionalized bioelectroactive surfaces†

Danfeng Cao,[a] Mohammad Javad Jafari,[b] Erik Hultin,[c] Anton Nordin,[a] Jacob Rönnqvist,[a] Yusheng Yuan,[d] Emma Rörby,[c] Jan-Ingvar Jönsson,[c] Thomas Ederth,[b] Jose G. Martinez[a] and Edwin W. H. Jager *[a]

Hematopoietic stem cells (HSCs) are rare cells residing in the bone marrow and give rise to millions of new blood cells daily throughout life. Because of their multipotent, self-renewing nature, they have also been used for several decades to treat hematological disorders. However, HSCs are scarce and difficult to maintain *ex vivo*, demonstrating the need for developing novel *in vitro* methods to expand HSCs that mimic the complex *in vivo* microenvironment in suitable culture tissue plates, in extracellular matrix scaffolds, or on a biochip. One component to include in such an artificial microenvironment is HSC-related growth factors (GFs) immobilized on surfaces that mimic membrane-bound GFs *in vivo*. In this paper, we have initiated the development of an *ex vivo* system to study the immobilization of growth factors that sustain HSC maintenance and possibly expansion. However, since HSC-related GFs are expensive we have developed a proof-of-concept model using bovine serum albumin (BSA) as an alternative. Polypyrrole (PPy) was electrochemically synthesized in the presence of dicarboxylic acids with different hydrocarbon chain lengths and polycarboxylic acids with different molecular weights as dopants. BSA was immobilized on the PPy surface using 1-ethyl-3-(3-dimethylaminopropyl) carbodiimide hydrochloride (EDC) and *N*-hydroxysuccinimide (NHS) to couple BSA to the carboxylic acid dopant of PPy. These PPy films with different dopants showed different abilities to immobilize BSA using EDC/NHS coupling and also different surface properties. In addition, owing to the interesting switchable properties of PPy upon alteration of the oxidation/reduction potential, the immobilized BSA could change its presentation on the PPy surface depending on the redox state. To characterize the PPy surfaces and to study the different immobilization results of BSA on these PPy variants with different dopants and different presentation behavior upon redox switching, the electrochemical properties, hydrophobicity, thickness, roughness, surface COOH density and fluorescence labeling were investigated. The results indicate that the polycarboxylic acid dopants could immobilize more BSA on the PPy surface. Moreover, the BSA in the as-fabricated state shows a "collapsed" presentation on the PPy surface, a "less collapsed" presentation in the oxidized state and an "erected" presentation in the reduced state. Cell viability studies using hematopoietic cells showed that the developed PPy-BSA surfaces did not negatively alter cell viability or cell proliferation compared to the control.

Received 20th June 2024,
Accepted 13th December 2024

DOI: 10.1039/d4lp00207e

rsc.li/rscapplpolym

1 Introduction

Hematological disorders are diseases that affect the blood and the organs that produce blood in various ways. Leukemia, myeloma, and lymphoma are three kinds of cancers that are classified as hematological disorders. Each year, these three malignancies account for approximately 6.6% of cancer cases worldwide.[1] The overall 5-year survival for blood cancer is around 70%, leaving many patients to succumb to the disease. Leukemia, myeloma, and lymphoma are commonly treated with chemotherapy, radiation treatment, stem cell transplan-

[a]*Sensor and Actuator Systems, Department of Physics, Chemistry and Biology (IFM), Linköping University, Sweden. E-mail: edwin.jager@liu.se*
[b]*Biophysics and Bioengineering, Department of Physics, Chemistry and Biology (IFM), Linköping University, Sweden*
[c]*Department of Biomedical and Clinical Sciences (BKV), Linköping University, Sweden*
[d]*Electronic and Photonic Materials, Department of Physics, Chemistry and Biology (IFM), Linköping University, Sweden*

† Electronic supplementary information (ESI) available. See DOI: https://doi.org/10.1039/d4lp00207e

tation (SCT), or a combination of these methods. SCT is classified into two types: allogeneic and autologous.[2] The most preferred method is allogenic transplantation because of its potential for the graft-*versus*-tumor effect, which implies that the transplanted cells aid in the fight against any leftover tumor cells in the recipient's body following chemo- or radiation therapy. The graft-*versus*-tumor effect, however, does not occur with autologous SCT since the stem cells come from the patient, and they may still be influenced by the disease. However, there is a difficulty with allogeneic transplantation: there is a scarcity of hematopoietic stem cells (HSCs) that match the recipient's human leukocyte antigen (HLA) type. HLAs are membrane-bound proteins that must match the HLA type of the recipient in order for the body to accept the donor HSCs. As a result of the scarcity, there is a great need for allogeneic stem cells that can be matched to any recipient.[3,4] Scientists have attempted to genetically modify these HSCs to match the recipient HLA; however, due to their scarcity, these modified HSCs cannot be employed for leukemia treatment. *Ex vivo* HSC expansion has been attempted to treat hematological malignancies, albeit with limited success. This is due to the issue of the complex microenvironment, or niche, that regulates HSC self-renewal, migration, differentiation, and homing.[3–5] It has been demonstrated that HSCs in distinct bone marrow regions have different self-renewal capacities and that HSCs shift location with aging, thereby altering their niche during development.[3,4] Hence, it is necessary to develop an *ex vivo* platform, like a smart culture dish or a biochip, for cell cultivation and expansion. Although short-term survival and expansion of HSCs *in vivo* have been achieved, the long-term *in vitro* expansion for clinical studies and use is still a challenge.[6] Therefore, developing a "bioelectroactive surface" to modulate cellular behavior in such a complex microenvironment would be an alternative method, where one way would be to design this kind of "bioelectroactive surface" to create an interface with immobilized GFs on polymer films.[7]

Conducting polymers (CPs) or conjugated polymers are organic semiconductors. CPs exhibit properties like redox activity and combined electrical and ionic conductivity. Moreover, with the finding of biological compatibility, CPs established their niche in biomedical fields, such as in tissue engineering, and organ-on-chips.[8,9] They have been used in the long-term study of regulation and controlling (stem) cells *in vitro*.[10–12] In addition to the conductive properties derived from their doped molecular structure, CPs have a high degree of adaptability due to the possibility of selecting among a large number of dopants and modifying them by covalently adding side groups.[13] More importantly, the surface properties of CPs can be electronically tuned and switched, which is a crucial merit for controlling the biological activity of cells.[14,15] One of the most studied CPs is PPy, which is a good choice for creating an *in vitro* microenvironment due to its typical properties of CPs, *e.g.*, good electrical conductivity, hierarchical structure and tunability of the surface.[16] Liao *et al.* reported that the PPy surface characteristics, such as wettability, can be tuned or controlled by electrochemical switching between its oxidized and reduced states.[15] This surface characteristic change of PPy is caused by counterion injection/ejection, conformational changes of the polymer chains and oxidation/reduction of the polymer backbone during redox switching. The redox reactions including ion motion for p-doped PPy with small mobile dopants are described using eqn (1) or with large immobile dopants using eqn (2).[17,18]

$$\mathrm{PPy^+(a^-) + e^- \leftrightarrow\ Ppy^0 + a^-(aq.)} \quad (1)$$

$$\mathrm{Ppy^+(A^-) + c^+(aq.) + e^- \leftrightarrow\ Ppy^0(A^-c^+)} \quad (2)$$

where a^- is the small mobile anion, A^- is the large immobile anion, c^+ is the small cation, and e^- is the electron. This switching of the surface properties would provide potential applications in culturing and studying HSCs *in vitro*.[6] Critical biomolecules for HSCs are growth factors (GFs) and cytokines that can be found in the native HSC niches *in vivo* and are used in cell culture media for HSC expansion *in vitro*, which include stem cell factor (SCF), thrombopoietin (TPO), and interleukin-3 (IL-3). Hence, to study the effect of redox switching of the electroactive surface on these biomolecules on the surface and their subsequent effect on the culturing of HSCs, these critical biomolecules need to be immobilized on the PPy surface.

Two approaches can be used to immobilize biomolecules on surfaces: physical and chemical immobilization, respectively. The physical immobilization methods include the adsorption of biomolecules onto a substrate or entrapment or encapsulation into a matrix or scaffold. For instance, Hameed *et al.* encapsulated insulin-like growth factors into poly(lactic-*co*-glycolic acid) microparticles for cardiac application studies.[19] Surface adsorption is one of the simplest methods to immobilize biomolecules on surfaces. This method has been utilized to immobilize different kinds of GFs, such as BMP-2, FGF, and FGF-2.[20,21] The disadvantages of the physical immobilization method are low loading efficiency, poor control over binding and subsequent release, and minimum spatial control.[22,23] The chemical immobilization method relies on attaching biomolecules through covalent bonds directly to the substrate surface using functional groups in the biomolecule. For instance, Baumgartner *et al.* immobilized IL-3 onto the PPy surface using EDC/NHS covalent coupling to facilitate the reaction of the $-NH_2$ group in IL-3 with the COOH group of the dopant in PPy.[6] Place *et al.* immobilized GFs to a hydrogel *via* a thiol coupling immobilization approach.[24] Gomez *et al.* used a light-induced covalent method to immobilize GFs on PPy using arylazido-containing compounds under UV light by creating singlet nitrenes to achieve immobilization.[11]

Different carboxylic acids were used as dopants in PPy by Baumgartner *et al.* to couple biomolecules containing amine groups using the EDC/NHS technique.[6] They used dopants with two COOH groups to ensure that there is always a COOH group available for the coupling chemistry, where one COO^- group compensates the polaron on the PPy backbone and another one could protrude out of the surface available for

immobilization. They immobilized IL-3, a cytokine discovered as a soluble protein in the HSC niche, on the PPy surface and dynamically switched the presentation of immobilized cytokines to mimic biological stimulation, which was shown to affect HSC cell viability. The PPy samples doped with carboxyl groups in Baumgartner *et al.* provided limited control over the number of carboxyl groups since the dopants are dicarboxylic molecules and have short hydrocarbon chains, resulting in few carboxylic acid molecules available for protein immobilization.

Baumgartner *et al.* showed that FDC-P1 hematopoietic progenitor cells can be cultured on these carboxylic acid-doped polypyrroles for 48 h, thus indicating good cell viability.[6] They evidenced that IL-3 is an important cytokine for stimulating the proliferation of HSCs. SCF is another cytokine that plays an important role in hematopoiesis to support the survival and differentiation of HSCs and progenitor cells. Unlike IL-3, SCF is identified as a membrane-bound protein. This is desirable because it more closely resembles the HSC niche. SCF, on the other hand, is very expensive and thus unsuitable to use for developing and testing various immobilization techniques. BSA is a low-cost model protein with well-known physicochemical properties and is therefore widely used in basic research.[25–29] BSA as a model protein is composed of the basic structure of amino acids, consisting of a 580 amino acid residue globular protein with 17 intrachain disulfide links and one free thiol group at position 34.[30,31] Its secondary structure is composed of approximately 54% α-helices and 40% β structure and includes three binding domains that are specific for metal ions, lipids, and nucleotides, respectively.[32] BSA belongs to the soft protein class, which may easily alter its structure and shape,[30] similar to our target molecules.[6] Therefore, BSA is used as a model instead of SCFs in this study.

We introduce polycarboxylic acids with varied molecular weights not only for doping PPy but also to provide more functional carboxylic acid groups for the immobilization of BSA on the surface to increase the amount of immobilized BSA, as compared to the previous work by Baumgartner *et al.* Next, electrochemical switching of PPy doped with different polycarboxylic molecules and functionalized with BSA is used to explore the change in the presentation of BSA upon such redox switching.

2 Experimental

2.1 Materials

Pyrrole (Fluka, Switzerland) monomers were vacuum distilled and stored at −20 °C prior to use. Pyrrole-3-carboxylic acid (PyCOOH), oxalic acid (OXA), succinic acid (SUCA), poly(acrylic acid, sodium salt) solution, average $M_w \sim 1200$, 45 wt% in H_2O (PAA1200), poly(acrylic acid sodium salt), average $M_w \sim 2100$ (PAA2100), poly(acrylic acid, sodium salt) solution, average $M_w \sim 8000$, 45 wt% in H_2O (PAA8000), potassium chloride (KCl), lithium perchlorate ($LiClO_4$), sodium carbonate (Na_2CO_3), bovine serum albumin (BSA) and albumin–fluorescein isothiocyanate conjugate (FITC-BSA) were purchased from Sigma-Aldrich. The amine coupling kit with 1-ethyl-3-(3-dimethylaminopropyl) carbodiimide hydrochloride (EDC) and *N*-hydroxysuccinimide (NHS) was purchased from Cytiva (MA, USA). Deionized water (DI, 18.2 MΩ cm) was obtained from a Milli-Q Plus water equipment and used throughout the experiments.

2.2 Preparation of the polypyrrole surface

Prior to the polymerization of the polypyrrole films, gold-silicon (Au/Si) surfaces were fabricated by thermal evaporation (25 Å Ti adhesion layer and 1000 Å Au on a Si wafer), cut into 1 cm × 2 cm pieces, cleaned with an RCA1 solution (25% ammonia, 30% hydrogen peroxide solution and deionized water in a 1 : 1 : 5 ratio) for 10 minutes at 85 °C, rinsed with DI water and dried with nitrogen. Polypyrrole films were synthesized on Au/Si by electropolymerization using a three-electrode setup consisting of immersing a 1 cm × 1 cm area of the Au/Si surface into the electrolyte as the working electrode, a stainless steel mesh as the counter electrode, and a BASi MF-2052 Ag/AgCl (3 M NaCl) reference electrode (RE). The electrochemical polymerization of PPy with COOH side groups on the Au/Si surface was performed using a constant potential of +1.25 V in an aqueous solution of 0.1 M Py-COOH (Fig. 1) containing 0.1 M $LiClO_4$ and 0.1 M Na_2CO_3 until 50 mC synthesis charge was consumed. This sample is denoted as PPyCOOH. Regular (*i.e.*, non-substituted) PPy with five different types of counterions was synthesized by mixing the counterion (0.1 M OXA, 0.1 M SUCA and 0.1 M carboxylic acid concentration for PAA1200, PAA2100 and PAA8000) with 0.1 M pyrrole monomers and thin polypyrrole films were electrochemically synthesized on the Au/Si substrates by applying a constant potential (+0.6 V for OXA and SUCA, +0.7 V for PAA1200, PAA2100 and PAA8000) to the working electrode until 50 mC synthesis charge was consumed.[6] These samples are named PPy(OXA), PPy(SUCA), PPy(PAA1200), PPy(PAA2100) and PPy (PAA8000). PPyCOOH and all non-substituted polypyrroles doped with these counterions are denoted as PPy. After synthesis, the samples were washed with DI water, then dried with nitrogen, and stored at room temperature.

2.3 Immobilization of BSA on the PPy surface

BSA was immobilized on the PPy surface using the EDC/NHS coupling technique. EDC (400 mM) and NHS (200 mM) from the kit were mixed in DI water before all experiments. PPy surfaces with carboxylic acid groups were activated by a 50 μl EDC/NHS mixture (1 : 1 ratio) for 50 minutes at room temperature. Surfaces were washed with DI water and thereafter incubated with 100 μl of 0.1 mg ml^{-1} BSA or 0.1 mg ml^{-1} FITC-BSA in DI water for 2 hours at room temperature and under dark conditions. The BSA-immobilized PPy surfaces were then washed with DI water for 30 minutes to remove excess, unbound BSA, dried at room temperature, and finally stored in a dark box. The immobilization route is shown in Fig. 1. Note: PPyCOOH and all PPy doped with the OXA, SUCA, and PAA series after immobilization with BSA are denoted as PPy-BSA.

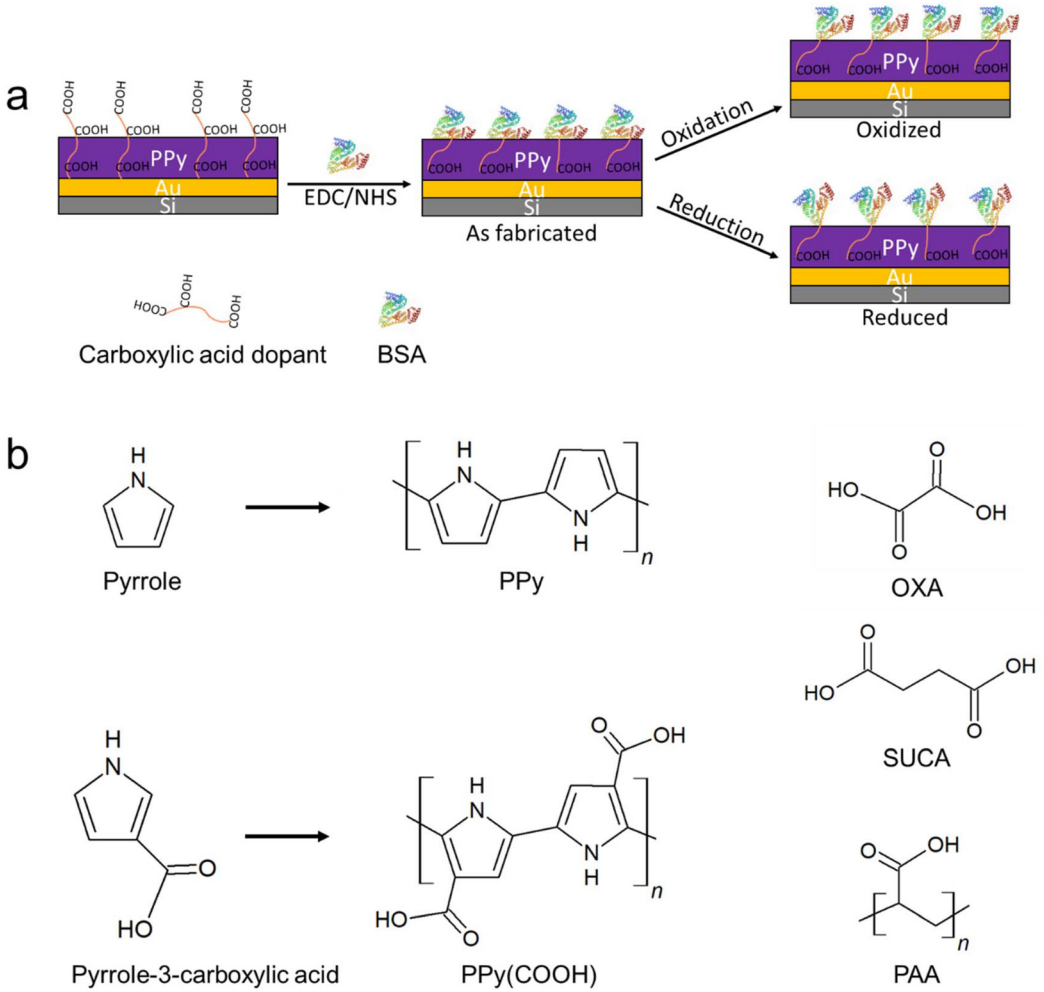

Fig. 1 (a) Illustration of the route of immobilization of BSA on the PPy surface and the presentation change of BSA in different redox states of PPy; (b) structure of pyrrole, PPy, pyrrole-3-carboxylic acid, and PPy(COOH), and the dopants used for electropolymerized PPy: oxalic acid (OXA), succinic acid (SUCA), and poly(acrylic acid) (PAA).

2.4 Electrochemical oxidation and reduction

For switching the presentation of the immobilized BSA, a constant positive (+0.8 V for PPyCOOH and +0.3 V for PPy with the other dopants) or a constant negative (−0.7 V) potential was applied to the PPy surface for 4 hours in 0.2 M KCl aqueous solution using the three-electrode setup as mentioned above.

2.5 Characterization

Electrochemical characterization using cyclic voltammograms (CV) of PPy surfaces was performed using an IviumStat.XR potentiostat controlled by the dedicated software (Ivium, Eindhoven, Netherlands). CVs were measured in 0.2 M KCl with a scan rate of 50 mV s^{-1} for 4 cycles. The second cycle was used in this study. The thickness of PPy surfaces was measured using a Dektak 6 M profilometer (Veeco Instruments Inc., NY, USA). The wettability (static angles) of the PPy surface was studied by water contact angle (WCA) measurements using a CAM200 Optical Contact Angle Meter (KVS Instrument, Helsinki, Finland). Atomic force microscopy (AFM) measurements with tapping mode were performed using a Digital Instruments Dimension 3100 atomic force microscope (Bruker, Santa Barbara, USA) and 10 μm area scans of the samples' surface were conducted. The roughness (R_a) values of the PPy surfaces were calculated from the AFM measurement using Nanoscope Analysis 1.8 software. Scanning electron microscopy (SEM) images were collected using a Sigma-300 lens (Zeiss, Germany).

Fourier transform infrared reflection–absorption spectroscopy (FT-IRAS) was used to determine the chemical structure of samples. A Vertex 70 (Bruker, USA) system with a custom-built accessory for IRAS was used, with an incidence angle of 85° and a liquid nitrogen-cooled mercury cadmium telluride detector. This was used to assess BSA immobilization and monitor conformational changes in different redox states. All samples were prepared on 20 × 40 mm^2 gold-coated Si substrates. IRAS measurements were performed in three steps. First, spectra were captured from the PPy samples, and then,

spectra were captured from NHS-coupled PPy. Finally, spectra from the latter samples incubated in BSA were obtained. PPy spectra were subtracted from the spectra from the same samples after incubation in BSA to obtain the BSA spectra. Component band fitting in the amide I region (1750–1600 cm^{-1}) of the spectra was used to identify and quantify secondary structure elements of the proteins. We used second derivatives to find the band positions to feed into the fitting process.

Toluidine blue O (TBO) staining was performed to evaluate the surface density of carboxylic acid groups on the PPy and PPy-BSA surfaces.[33] In brief, PPy and PPy-BSA surfaces (1 × 1 cm^2) were incubated in 0.1 mM KOH solution containing 2 mM TBO for 2 h. The carboxylic acid groups deprotonate and the positively charged TBO molecules attach to them in a 1 : 1 ratio in the alkaline solution. The PPy and PPy-BSA surfaces were then extensively washed with 0.1 mM KOH solution for 10 minutes to eliminate the nonspecifically bound TBO molecules. Finally, the TBO-attached molecules were desorbed by immersing them in 3 mL of 50% acetic acid for 30 minutes before performing absorbance spectroscopy at 631 nm with a UV-vis spectrophotometer (UV-2450, Shimadzu, Japan). A fluorescence microscope Ti–E (Nikon, Japan) was used to examine the BSA fluorescence images in different redox states. Image J (Ver. 1.4.3.67, USA) was used to calculate the intensity of fluorescence-labeled FITC-BSA.

All characterizations were performed three times using different samples, except for the fluorescence, which was measured three times using the same sample.

2.6 Cell viability

Animals were housed in the animal facility at Linköping University and the experiments were reviewed and approved by the Linköping Animal Ethical Committee. Bone marrow cells were isolated from the femur and tibia of sacrificed 11-week-old male C57bl9-J mice by crushing the bones in phosphate-buffered saline (PBS) (Cytiva) using a pestle and mortar. Bone fragments were separated from the cell suspension by filtering the solution through a 70 μm nylon mesh (Thermo Fisher Scientific, MA, USA). Red blood cells were lysed (StemCells Technologies, Vancouver, Canada), followed by Fc-block (3/100, 93) (BioLegend, CA, USA) for 5 minutes at room temperature and antibody staining with anti-CD45 (30-F11, FITC, 1/100) (BioLegend), anti-c-KIT (2B8, PE, 1/100) (BioLegend), and Live/Dead Fixable Near IR (780) Viability Kit (0, 2/1000) (Thermo Fisher Scientific) for 20 minutes at 6 °C, before sorting for live $CD45^+$ $c\text{-}KIT^+$ hematopoietic cells using the BD FACSAria III (BD Biosciences, NJ, USA).

Sorted cells were cultured in a 48-well plate (SPL Life Sciences, Pocheon, South Korea). The bottom of each well was blank (control) or covered with an OXA, SUCA, PAA1200, PAA2100, or PAA8000 doped PPy-BSA surface. Each well contained cells at a concentration of 1×10^5 ml^{-1} in a StemSpan Serum-Free Expansion Medium (SFEM) (StemCells Technologies) containing SCF, TPO, Fms-related tyrosine kinase 3 ligand (FLT3L) (50 ng ml^{-1}) and interleukin-6 (IL-6) (10 ng ml^{-1}) (all from Thermo Fisher Scientific) and the incubation lasted for 48 hours under 37 °C, 5% CO_2, and 99% humidity conditions.

After 48 hours all wells were washed with PBS and the cell suspension was stained with Fc-block (98, 3/100) for 5 minutes at room temperature followed by anti-CD45 (30-F11, FITC, 1/100), anti-c-KIT (2B8, PE, 1/100), and the Live/Dead Fixable Near IR (780) Viability Kit (0, 2/1000) for 20 minutes at 6 °C. Cell numbers and vitality were analyzed using the Cytek Aurora (Cytek Biosciences, CA, USA) spectral cytometer.

3 Results and discussion

3.1 Immobilization of BSA on PPy films

We prepared PPyCOOH and PPy films doped with the different dopants with varied carbon chain lengths of polycarboxylic acid using the electrosynthesis method to tailor the distance between the immobilized protein and the PPy surface. The carboxylic acid dopants were chosen due to their good capacity to immobilize proteins where their carboxy ends can couple with amino groups from the protein using EDC/NHS coupling.[6] To determine the surface characteristics and successful immobilization of BSA on the PPyCOOH and PPy surfaces, electrochemical properties, IRAS, and surface morphology were measured.

The electrochemical properties of PPy and PPy-BSA were investigated by cyclic voltammetry (CV) in 0.2 M KCl solution. As shown in Fig. 2, the voltammograms for PPy doped with OXA, SUCA, PAA1200, PAA2100, PAA8000 and their PPy-BSA samples show the classical CV shape with one pair of redox peaks, which also exhibit differences in conductivity and redox performance, while the PPyCOOH and PPyCOOH-BSA samples show different kinds of CV shapes with four pairs of redox peaks. Fig. 2 shows that the current range of PPy-BSA was reduced compared to their equivalent unmodified PPy samples in most cases, except for PPyCOOH and PPy(PAA1200) and their BSA immobilized samples. Moreover, the reduction peaks of all PPy-BSA samples were shifted to lower potential compared to PPy samples, while the oxidation peaks of all PPy-BSA samples were shifted to higher potential compared to PPy samples as indicated by arrows in Fig. 2. The ion transfer between the PPy surface and the electrolyte might be impeded by the immobilization due to physical blockage and/or the charged groups of BSA, hence a lower current and a bigger separation between the redox peaks.

The IRAS spectrum of BSA shown in Fig. 3 provides detailed information about the secondary structure of BSA, corresponding to its functional groups. A broad band centered around 3300 cm^{-1} (amide A) is observed, along with several bands between 3000 and 2800 cm^{-1}, which are attributed to N–H stretching of primary amines and C–H vibrations, respectively.[34] Three main peaks, corresponding to amide I (C═O stretching), amide II (N–H bending and C–N stretching) and amide III (N–H bending and C–N stretching), appear at 1674 cm^{-1}, 1548 cm^{-1} and 1240–1310 cm^{-1}, respectively.[34–36]

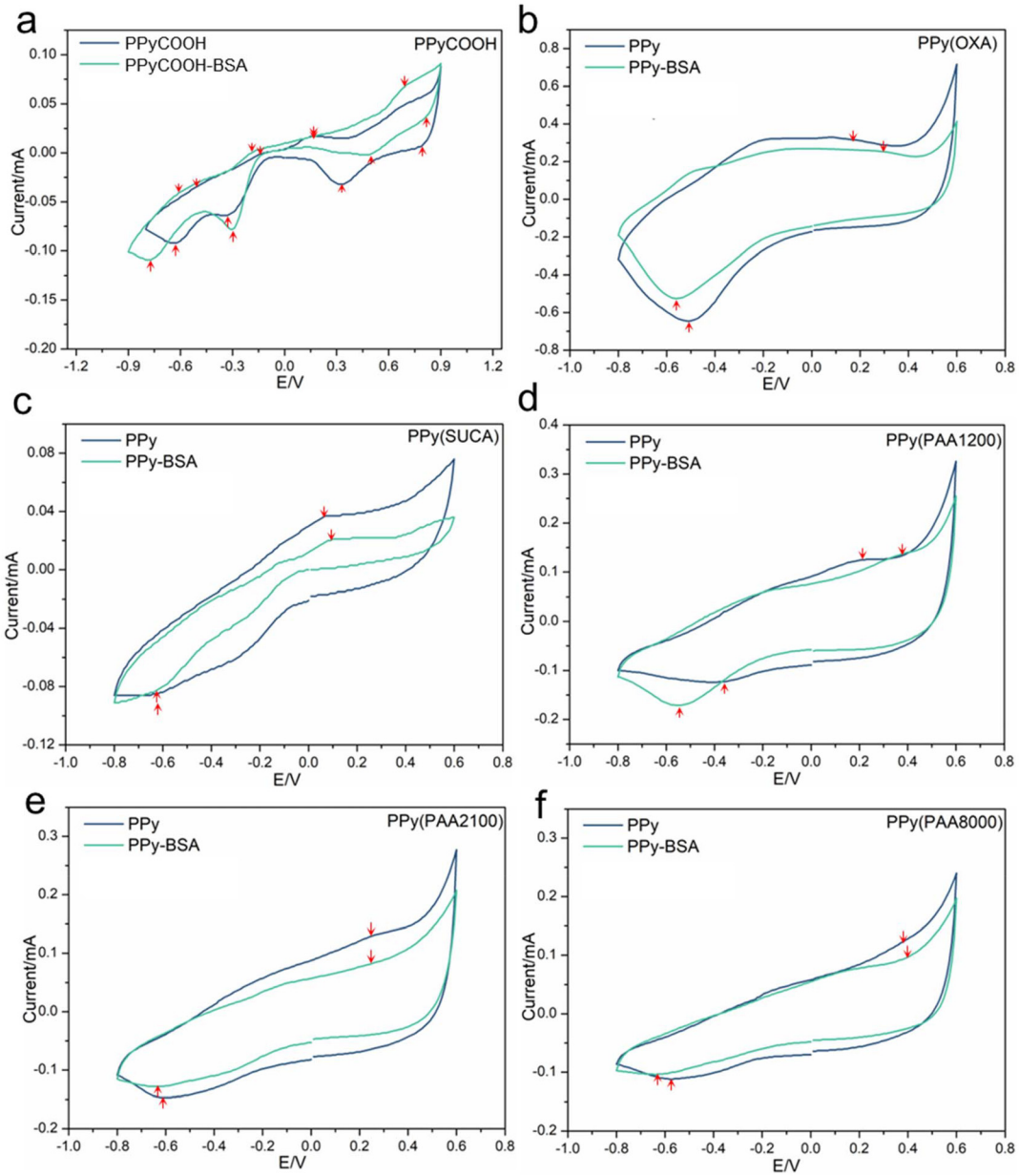

Fig. 2 CV results of PPy and PPy-BSA films. (a) PPyCOOH and PPyCOOH-BSA, (b) PPy(OXA) and PPy(OXA)-BSA, (c) PPy(SUCA) and PPy(SUCA)-BSA, (d) PPy(PAA1200) and PPy(PAA1200)-BSA, (e) PPy(PAA2100) and PPy(PAA2100)-BSA, (f) PPy(PAA8000) and PPy(PAA8000)-BSA. All measurements were made in 0.2 M KCl electrolyte at a scan rate of 50 mV s^{-1}.

The position and shape of these bands can provide insights into the secondary structure of the protein. The positions of the amide I and amide II bands, in particular, indicate a high α-helix content.[35,37] Other bands at 1454 cm^{-1} and 1394 cm^{-1} are related to CH_2 scissoring and CH_3 bending from side chains, respectively.[38,39]

IRAS spectra of PPy and PPy-BSA surfaces with different dopants are shown in Fig. 3. In the IRAS spectra of all samples, peaks in the range close to 1711 cm^{-1} (area I in Fig. 3, black lines) can be seen from C═O vibrations in the carboxyl groups of the different carboxylic acid dopants in PPy. The corresponding peak in PPyCOOH originates from the carboxylated monomers (see Fig. 1).[40] The broad band over 1509–1634 cm^{-1} (area II in Fig. 3, black lines) which can be seen in all samples is the characteristic absorption for the pyrrole ring double bond vibration.[41] In Fig. 3, the PPy-BSA samples doped with OXA, SUCA, and PAA series showed increased amide I band C═O stretching (area I in Fig. 3, red lines), as well as increased amide II bands from C–N stretching and N–H bending (area II in Fig. 3, red lines) and amide N–H stretching at around 3400 cm^{-1}. For PPyCOOH-BSA, the amide I and amide II peaks are shifted to 1740 cm^{-1} and 1668 cm^{-1}.

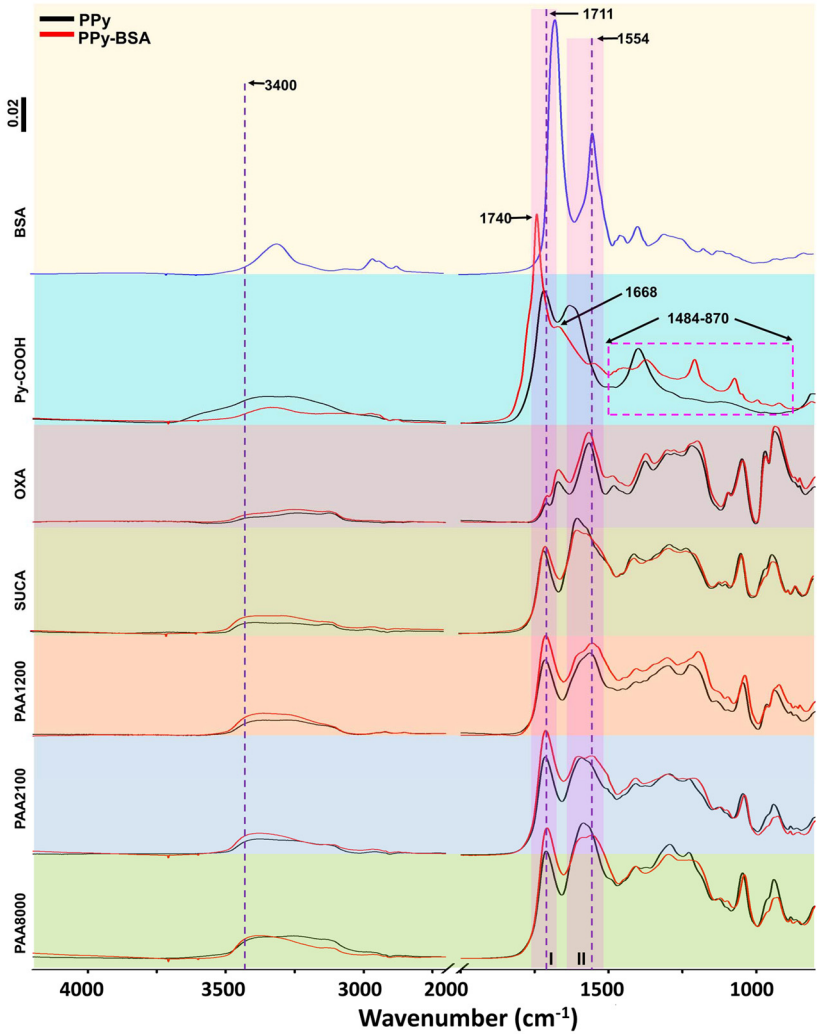

Fig. 3 IRAS results from samples with different dopants before (PPy) and after (PPy-BSA) BSA immobilization.

Moreover, some new peaks appeared for PPyCOOH-BSA (pink dashed area, 1484–870 cm^{-1}), which are attributed to residual NHS-ester, as shown in Fig. S1.† Overall, the IRAS spectra indicate that BSA is immobilized successfully on the PPyCOOH and PPy surfaces.

The surface roughness, thickness, and wettability are important surface characteristics. The different dopants used have a major effect on the surface roughness, thickness, and wettability of conducting polymers and these surface properties could also influence cell attachment or protein immobilization. The roughness, thickness, and wettability properties of PPy and PPy-BSA with the different dopants are shown in Fig. 4. The roughness results obtained from AFM measurement indicate that PPyCOOH had the smoothest surface (R_a = 1.08 nm), while PPy(OXA) (R_a = 2.5 nm) and PPy(SUCA) (R_a = 3.32 nm) had a little higher roughness than PPyCOOH, but these three samples were still smooth. However, for the PPy (PAA) samples doped with polycarboxylic acids (PAA) of different molecular weights, the roughness increased 10-fold compared to those with shorter carbon chain length dopants and reached 24.5 nm for PAA1200, 23.8 nm for PAA2100, and 19.5 nm for PAA8000, respectively. The roughness values of the corresponding PPy-BSA surfaces also increased notably compared to the plain PPy surfaces. Because BSA is a relatively large protein, its attachment and immobilization could greatly change the surface characteristics. The surface thickness also presented a similar tendency of increase due to the immobilization of BSA on PPy surfaces, as shown in Fig. 4b. Variations in the wettability with the different dopants of PPy before and after BSA immobilization are displayed in Fig. 4c. PPy electropolymerized with different dopants showed totally different water contact angles (13 ± 1° for PPyCOOH, 65 ± 2° for PPy (OXA), 52 ± 3° for PPy(SUCA), 62 ± 3° for PPy(PAA1200), 39 ± 3° for PPy(PAA2100) and 53 ± 2° for PPy(PAA8000)) clearly showing the effect of the dopants on the wettability. On the other hand, after BSA immobilization, different surfaces exhibited similar water contact angles (about 68°). These similar water contact angles independent of the dopant mole-

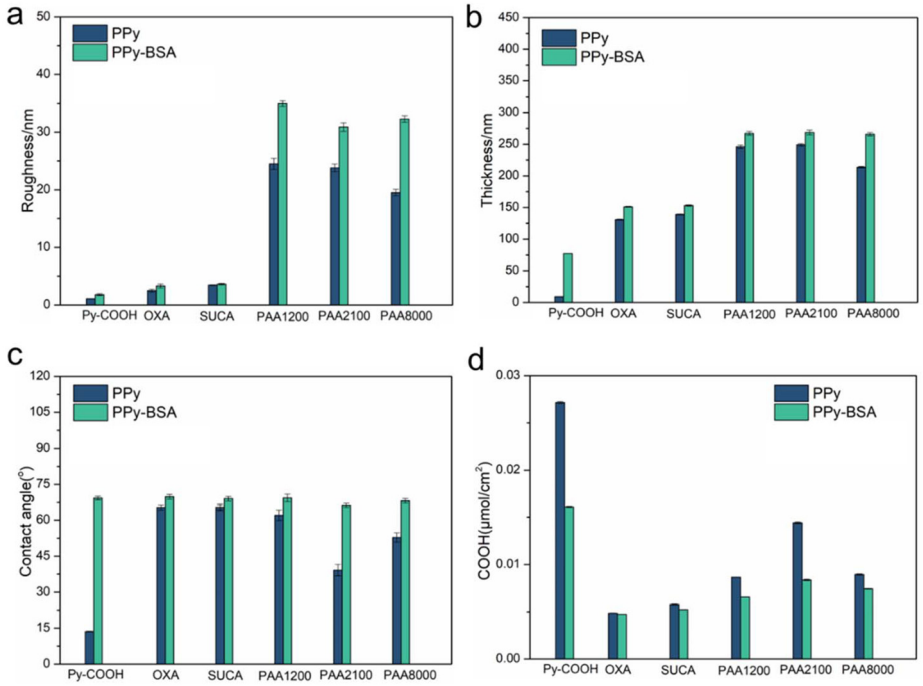

Fig. 4 Surface characterization of PPy and PPy-BSA films. (a) roughness (R_a), (b) thickness, (c) water contact angle, and (d) TBO staining results. Data represent mean ± standard deviation.

cules clearly indicate that the BSA covered the PPy surface in all samples. A similar WCA of 76° was obtained on magnesium surfaces, which were modified with BSA and ascorbic acid.[42] In contrast, the water contact angle of non-specifically adsorbed BSA on PPy is ~57°, lower than the covalently bound BSA, indicating that there is some non-specific adhesion of BSA on non-modified PPy, but the EDC-NHS mediated covalent coupling leads to much more BSA addition (Fig. S2a and b†).

The overall surface density of carboxylic acid groups on the PPy and PPy-BSA surfaces was assessed using the toluidine blue O (TBO) staining approach, which used the cationic dye toluidine blue O binding to negatively charged groups in a 1 : 1 ratio (*e.g.*, carboxylic acid group in this case).[33] The results in Fig. 4d show that PPyCOOH had the highest density of carboxylic acid on the surface. This is because the carboxylic acid groups of PPyCOOH are situated on the backbone of pyrrole-3-carboxylic acid, meaning each pyrrole monomer contributes one carboxyl group. A significant difference among the non-substituted PPy samples doped with various carboxylic acids can be noticed. On one hand, those PPy samples doped with short-chain dicarboxylic acids, such as PPy(OXA), showed the lowest amount of carboxylic acid and PPy(SUCA) showed the second lowest amount of carboxylic acid. On the other hand, all the PPy samples doped with PAA dopants with polycarboxylic acid chains showed higher carboxylic acid densities than PPy (OXA) and PPy(SUCA). This means that the polycarboxylic acids did increase the amount of exposed carboxylic acids out of the PPy surface, which could give more immobilization sites than the short-chain dicarboxylic acids. However, based on the theoretical number of carboxylic groups, the TBO value of PPy (PAA8000) should have been increased compared to PPy (PAA1200) due to the longer carbon chain length polycarboxylic acid, while the measured value of PPy(PAA8000) was lower than those of PPy(PAA2100) and similar to PPy(PAA1200).

Furthermore, the COOH values of PPy-BSA samples were lower than those of unmodified PPy samples, which indicates that the BSA immobilization process consumed many carboxyl groups by EDC/NHS covalent bonding, resulting in fewer remaining carboxyl groups capable of binding to TBO, further confirming BSA immobilization.

The morphology of PPy and PPy-BSA surfaces was characterized by scanning electron microscopy and atomic force microscopy. The microstructural features of the synthesized PPy and their corresponding PPy-BSA samples are shown in Fig. 5. It can be noticed from the SEM images that the surface morphology and nodular structures in PPy samples vary with various dopants used for their synthesis,[43–45] while the surface morphology and nodular structures between PPy and their corresponding BSA modified surfaces were similar. From the SEM pictures, PPyCOOH and PPyCOOH-BSA had very smooth surfaces with almost no significant nodules. PPy(OXA), PPy (OXA)-BSA, PPy(SUCA), and PPy(SUCA)-BSA showed a little higher roughness than PPyCOOH surfaces. However, from the AFM roughness measurement in Fig. S3,† we can see that their nodules were still very small (about 5 nm) and had comparable and homogeneous surfaces (Fig. 5b and c). Notably, the surfaces of PPy doped with PAA1200, PAA2100 and PAA8000

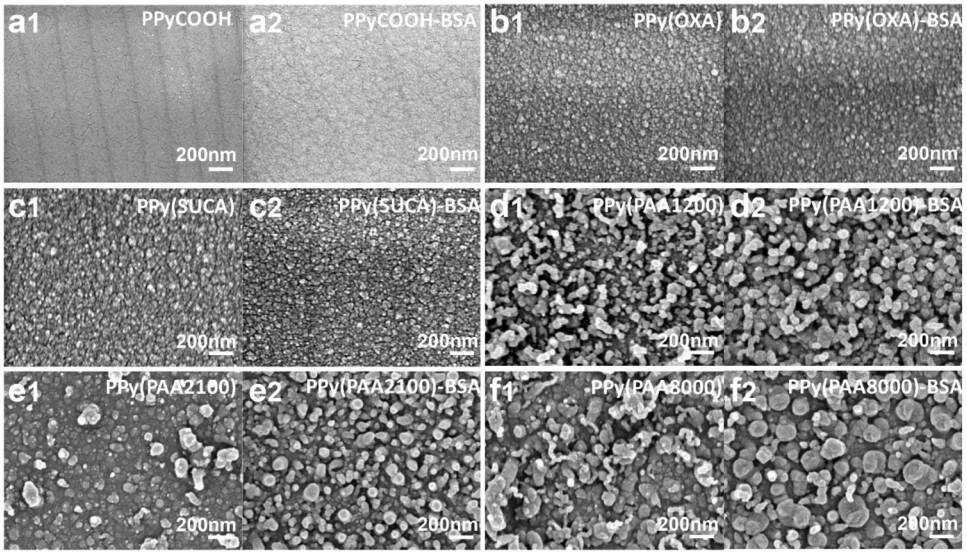

Fig. 5 SEM results of different dopants of PPy and PPy-BSA. (a1) PPyCOOH, (a2) PPyCOOH-BSA, (b1) PPy(OXA), (b2) PPy(OXA)-BSA, (c1) PPy(SUCA), (c2) PPy(SUCA)-BSA, (d1) PPy(PAA1200), (d2) PPy(PAA1200)-BSA, (e1) PPy(PAA2100), (e2) PPy(PAA2100)-BSA, (f1) PPy(PAA8000), and (f2) PPy (PAA8000)-BSA.

showed high roughness and larger size nodules but still had a homogeneous distribution (about 32 nm).[43,46] In line with what could be observed in the SEM results, the surface roughness and morphology of these samples are confirmed by profilometry (Fig. 4a) and AFM (Fig. S3†), respectively. The AFM can also take image measurements, and the images presented in Fig. S3† correspond to PPy samples and their corresponding PPy-BSA samples. The AFM images are presented in 2D format in Fig. S3,† clearly showing more white dots on the PPy surface after immobilization of BSA compared with PPy surfaces. It is well known from the literature that the immobilized BSA on the PPy surface can be imaged by means of AFM.[46–48] Hence, it indicates that these white dots are the immobilized BSA on the PPy surface.

To summarize, the above characterization studies by CV, IRAS, surface roughness, thickness, wettability, TBO and surface morphology were utilized for PPy and PPy-BSA surfaces. All the surface topographical properties changed after immobilizing BSA using the EDC/NHS method. The changes in the characterization results indicate that BSA was successfully immobilized on the PPy surfaces. The CV results indicate that the electrical conductivity of PPy-BSA is in the mA range, which is still sufficient to provide electrical control of cells' biological activity.[49] Moreover, the various surface morphologies obtained from different dopants enable diverse hierarchical structures to adjust the cellular response.[50]

3.2 Redox switching and change of BSA presentation on PPy films

Having verified that BSA was successfully immobilized on PPy surfaces, we investigated whether we could influence the BSA presentation upon redox switching of PPy-BSA. For this, we further studied the change in roughness, thickness, wettability, and electrochemical characteristics and used fluorescence imaging in the oxidized and reduced states by applying a positive and negative potential, respectively.

Fig. 6a shows the photographs of the six PPy-BSA surfaces with different dopants in the as-fabricated state (*i.e.*, unstimulated) and after oxidation and reduction by applying the redox potential for four hours. The pictures show that the surfaces in different redox states were still intact and that the films showed some color change (*i.e.,* electrochromism), except for the PPyCOOH-BSA surface where the PPyCOOH film dissolved after reduction and a dark-colored rim formed at the edge of the oxidized PPy film. The dissolution of the PPyCOOH-BSA surface in the reduced state is probably caused by the electrodissolution of the conducting polymer, *e.g.*, PPyCOOH in this case.[51–53] Thus, we excluded the PPyCOOH-BSA reduced state samples from any further experiments after those shown in Fig. 6. As shown in Fig. 6b, the roughness of PPyCOOH-BSA and unsubstituted PPy-BSA doped with OXA and SUCA was very low even in the oxidized and reduced states (lower than 5 nm). The PPy(PAA)-BSA surfaces were relatively rougher than the other three surfaces, but they still had a low roughness (lower than 45 nm). The volume change caused by the insertion/expulsion of ions led to a minor change in the roughness of these PPy(PAA) surfaces after applying the redox potential as shown in Fig. 6b.

The as-fabricated samples of the PPy(COOH), PPy(OXA), PPy(SUCA) and PPy(PAA) differed in thickness. The PPy(COOH) sample was the thinnest, followed by PPy(OXA) and PPy(SUCA) that had similar thicknesses. The as-fabricated samples PPy (PAA1200), PPy(PAA2100), and PPy(PAA8000), were the thickest and had similar thicknesses too. Although the thicknesses of

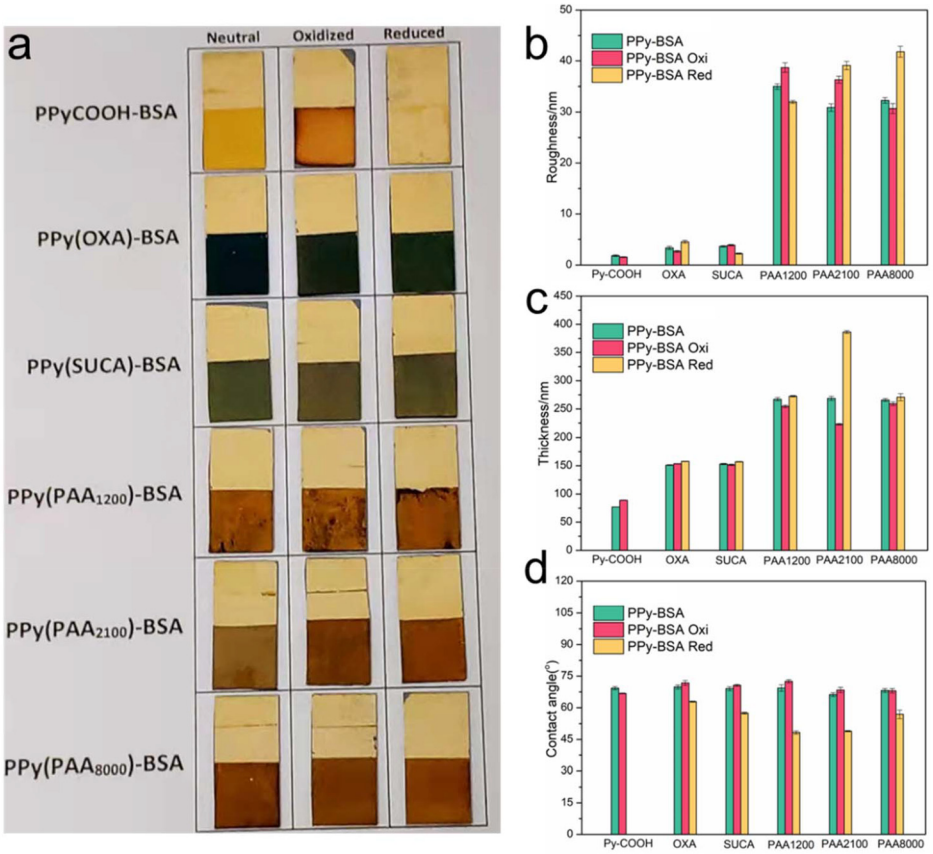

Fig. 6 (a) Photographs of PPy-BSA films in different redox states. The physical properties, (b) roughness, (c) thickness, and (d) wettability in different redox states. Note: PPy-BSA (as-fabricated/non-stimulated) gave the same results as shown in Fig. 4. Data represent mean ± standard deviation.

the PPy(PAA) series were similar in the as-fabricated state, their thicknesses varied for the corresponding oxidized/reduced states of PPy(PAA) samples. For the PPy surface doped with small mobile anions (*e.g.*, PPyCOOH surface), when the negative potential was applied to PPy, the electron incorporated into the PPy backbone and reduced the polymer, resulting in the expulsion of the small mobile anions to maintain charge neutrality and consequent shrinking of the film (following eqn (1)), but in this case, the film of PPyCOOH dissolved in the reduced state.[17] However, when a positive potential was applied to PPyCOOH, small anions from the electrolyte were inserted into the polymer matrix to keep charge neutrality, leading to a minor volume expansion (following eqn (1)). However, the PPy samples with large immobile anion dopants showed the opposite performance to the small mobile anion dopants. The PPy films doped with large immobile anions (PPy(OXA), PPy(SUCA) and PPy(PAA)) exhibited a volume expansion/contraction behavior caused by cation motion, following eqn (2). This behavior leads to an increase in the thickness in the reduced state and a decrease in the thickness in the oxidized state.[17,18,54] Thus, thickness changes shown in Fig. 6c are consistent with the reactions described in eqn (1) and (2). It can be noticed that PPy(PAA1200) showed a surprisingly large thickness change in the reduced state.

The variation in the wettability of the PPy surfaces with different dopants in different redox states was measured and is shown in Fig. 6d. We mentioned that the PPy-BSA samples prepared with different dopants showed a similar water contact angle of about 68° in the as-fabricated state. However, they presented different contact angles in oxidized and reduced states. PPyCOOH-BSA or PPy-BSA exhibited similar water contact angles in the oxidation and as-fabricated states, but the WCA in the oxidation state is a little higher than in the as-fabricated state. However, in the reduced state, the PPy-BSA samples attained a reduction of the WCA, *i.e.*, even more hydrophilic surfaces, and the WCA value in the reduced state decreased by 7° for PPy(OXA)-BSA, 12° for PPy(SUCA)-BSA, 21° for PPy(PAA1200)-BSA, 17° for PPy(PAA2100)-BSA, and 11° for PPy(PAA8000)-BSA samples compared to the as-fabricated states. This change of wettability could be caused by morphological or presentation changes of BSA on the surface as illustrated in Fig. 7. The WCA values of unmodified PPyCOOH and unmodified PPy surfaces in different redox states are shown in Fig. S4† and indicate a similar trend in the reduction in the WCA to that of PPyCOOH-BSA and PPy-BSA, but the difference between the redox states is larger for the unmodified samples than for the BSA samples. It can be noticed that PPy(PAA2100) also had a large reduction in the oxidized state, unlike the

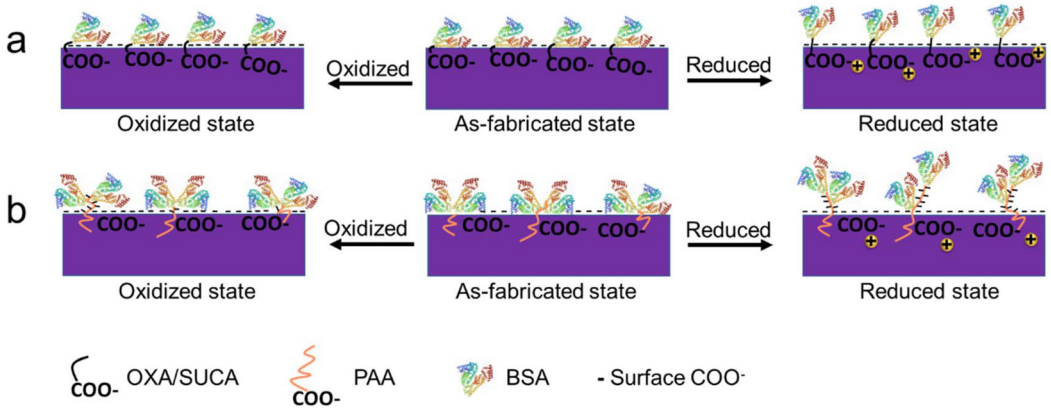

Fig. 7 A schematic illustration of the BSA presentation in different redox states. (a) BSA presentation and the number of exposed COO^- on redox PPy(OXA) and PPy(SUCA) surfaces; (b) BSA presentation and the number of exposed COO^- on the redox PPy(PAA) series surface.

other surfaces. It can be speculated that the BSA in the reduced state shows an "erected" presentation, resulting in most of the COO^- groups being exposed to water molecules, thus having the most hydrophilic property. The BSA in the oxidized state shows a similar "collapsed" presentation to the as-fabricated state; thus fewer COO^- groups are exposed.

To verify the change of the presentation state of the BSA on the PPy surfaces after switching the redox state, the TBO technique was again used. Fig. 8 shows that the COOH values of both oxidized and reduced state samples increased compared with the as-fabricated samples, but those of the samples in the reduced state were increased much more than the samples in the oxidized state, except for PAA1200 which had similar COOH values in both redox states. The increase in COOH values indicates that the presentation of BSA changed from "collapsed" presentation to "less collapsed" presentation to "erected" presentation after applying a positive/negative potential, thereby exposing more carboxylic acid groups in the BSA to bind with TBO. This indicates that both positive and negative potentials could change the presentation of BSA on the PPy surface, but the negative potential results in a greater change in the presentation of BSA, as shown in Fig. 7.

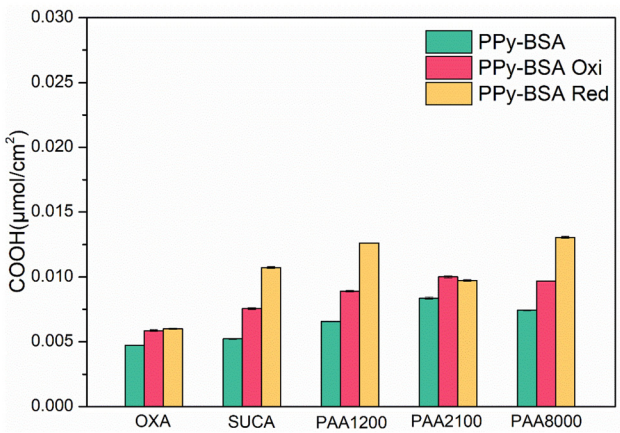

Fig. 8 COOH surface density of PPy-BSA in different redox states. Data represent mean ± standard deviation.

The oxidized samples showed higher COOH values than the samples in the as-fabricated state, which may be due to the opening of the spatial path between the collapsed BSA and the PPy surface by the transferred ions. The reduced state samples showed the highest COOH values because the "erected" presentation of BSA exposed more carboxylic acid of BSA. When the BSA presentation changes to the "erected" presentation in the reduced state or "less collapsed" presentation in the oxidized state, the space between the BSA and the PPy surface is released, leading to more COOH of dopants exposed to the TBO dye (Fig. 8), which also increased the COOH intensity. TBO results are consistent with wettability results.

BSA is a model protein, consisting of α-helix and β-sheet secondary structure. It is well known that β-sheet layers are flatter, thinner and more flexible than α-helices, suggesting that β-sheets would be better for building compact and sphere-wrapped shapes,[55] while the α-helices could be more fully extended than β-sheets.[56] Thereby, the BSA presentation could be fully extended when the BSA contains more α-helices, and the BSA presentation could be more compact when the BSA contains more β sheet layers. To investigate the conformational changes of BSA in different redox states, IRAS was used to estimate the α helix and β sheet structure contents of PPy-BSA samples. Fig. S5† and Table 1 show the content of α-helices and β-sheets of BSA in the different redox states. The results show that the BSA comprises more β-sheets in the as-fabricated state, which is similar but a little bit higher than the oxi-

Table 1 Ratios of the integrated areas representing β-sheet and α-helix contributions to the amide I IR bands of BSA in different redox states

(β1 + β2)/α integrated area (a.u)	OXA	SUCA	PAA1200	PAA2100	PAA8000
As-fabricated	1.35	1.12	0.77	1.11	0.70
Oxidized	1.25	0.96	0.69	1.08	0.54
Reduced	0.67	0.43	0.62	0.79	0.45

dized state, while the BSA comprises more α-helices in the reduced state. The different content of α-helices and β-sheet layers could further affect the presentation of BSA on PPy electroactive surfaces. α-Helices are loosened and extended, which results in the BSA being far away from the surface, while the β-sheet layers are compact and flatter, which easily results in the collapsed presentation. Hence, the IRAS results further indicate that the as-fabricated state has a "collapsed" presentation, the oxidized state shows a "less collapsed" presentation than the as-fabricated state and the reduced state shows an "erected" presentation.

Finally, we also used fluorescence measurements to verify the BSA presentation in the different redox states. Fig. 9 shows the fluorescence images of the PPy-BSA samples at the different redox states and the corresponding fluorescence intensities. The results exhibit that the as-fabricated PPy-BSA samples have large amounts of immobilized BSA on the surface. Their intensity values were between 3.10 (for PPy (OXA)) and 3.60 (for PPy(PAA1200)), much higher than those for the non-specific adsorption of BSA (Fig. S2†), again indicating appropriate immobilization of the BSA using covalent bonds. Investigating their change in the different redox states, PPy samples doped with OXA, SUCA or PAA dopants showed different trends. For OXA and SUCA samples, the intensity value was decreased, in order, from the as-fabricated to the

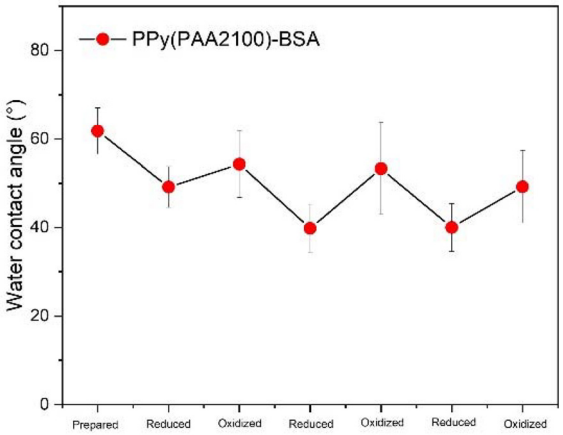

Fig. 10 The water contact angle of PPy(PAA2100)-BSA reduced and oxidized for 3 cycles showing reversible switching of the water contact angle and thereby the BSA representation.

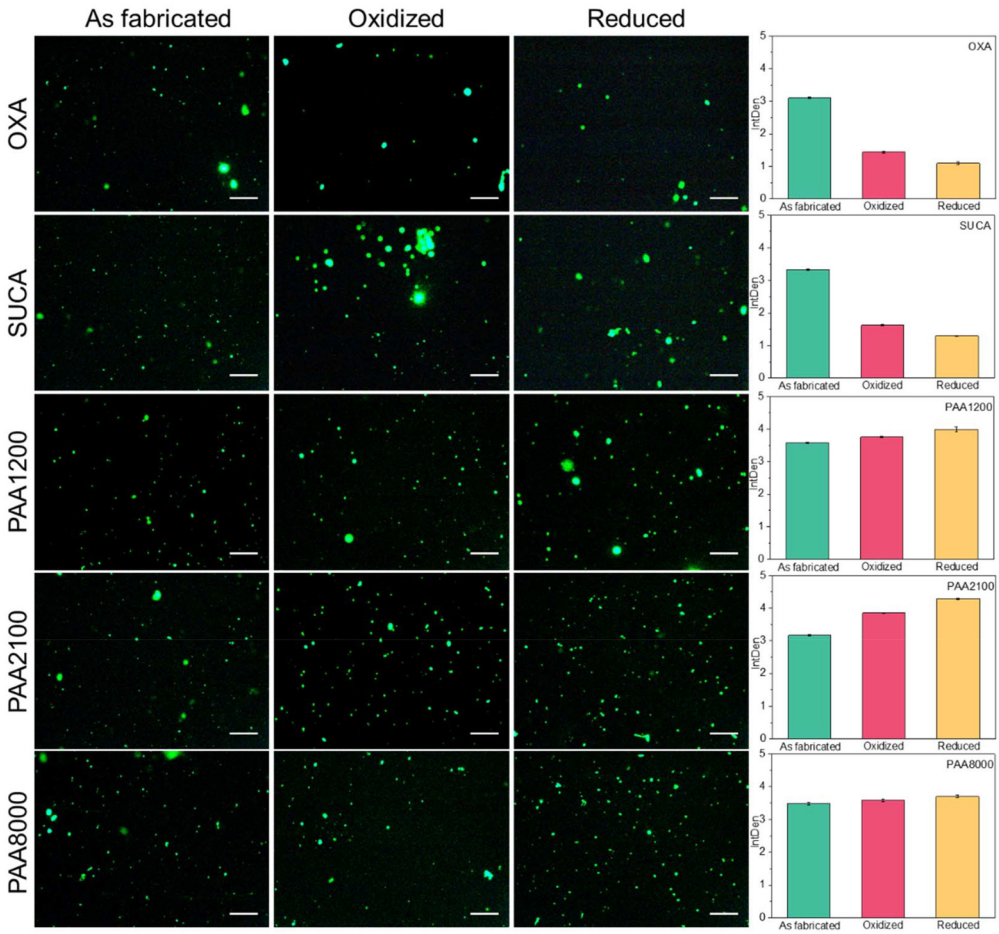

Fig. 9 Fluorescence images of PPy-BSA in the redox state. Data in the bar charts represent mean fluorescence intensity ± standard deviation. Scale bar is 250 μm.

oxidized state to the reduced state. OXA and SUCA are short-chain dicarboxylic acids and, therefore, may not be completely immobile anions. Thus, some of OXA and SUCA dopant ions present near the PPy surface may have the possibility to be released when redox potential was applied and ions transferred, and the immobilized BSA on those near-surface OXA and SUCA dopant molecules might also be lost along with those released carboxylic acid molecules. The decreased intensity values of PPy(OXA) and PPy(SUCA) may be caused by the loss of these near-surface, short dicarboxylic dopant molecules. The PPy(PAA) samples showed a totally different intensity trend for the various redox states as compared to dicar-

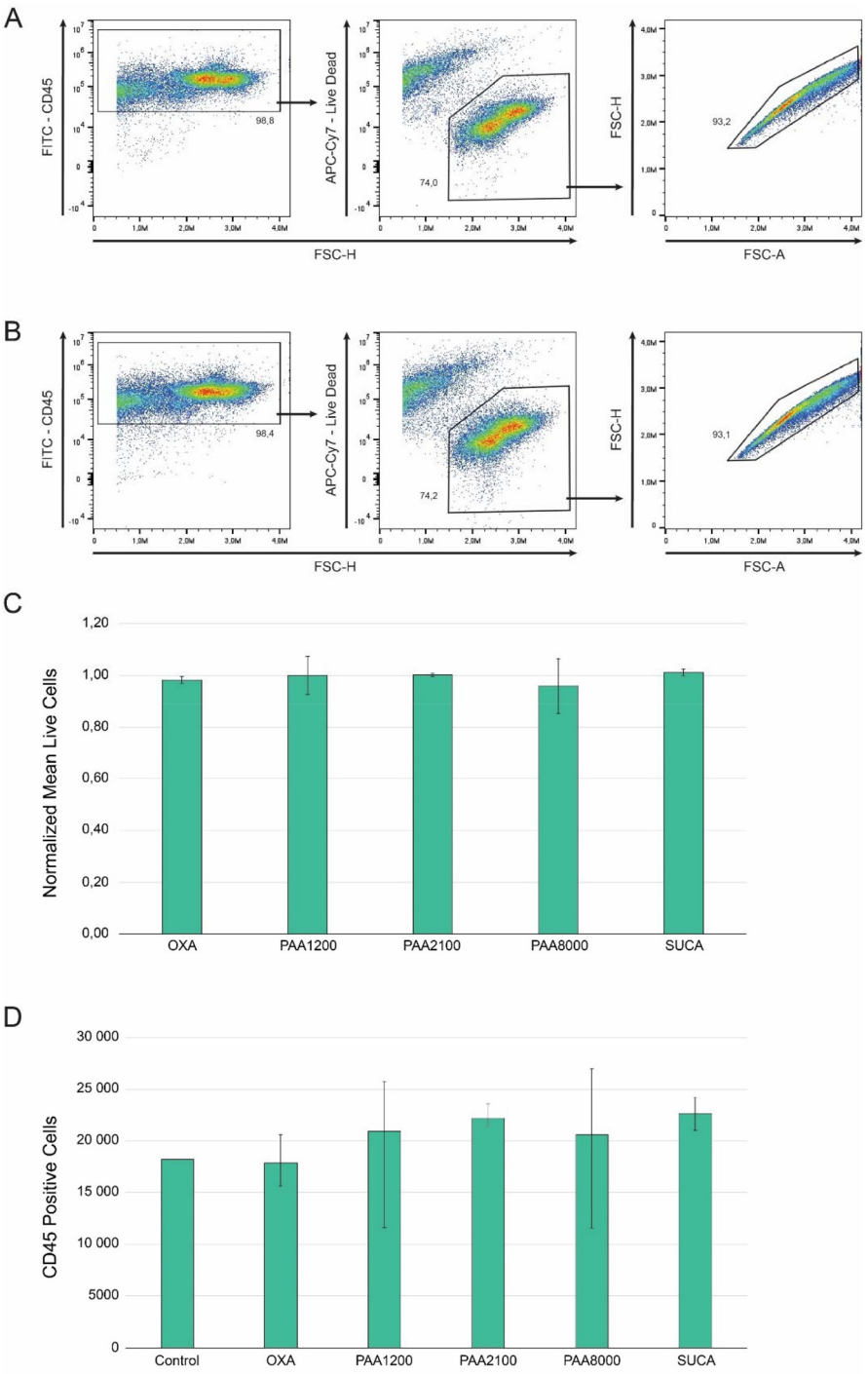

Fig. 11 Cell viability after 48-hour incubation. Representative gating of live CD45$^+$ cells in (A) control samples, and (B) PPy-BSA surfaces. (C) Cell viability normalized to the control. (D) Live CD45$^+$ c-KIT$^+$ hematopoietic cell number. Data in bar charts represent mean ± standard deviation.

boxylic acid-doped samples. The intensity values of PPy(PAA) samples increased in order from as-fabricated to oxidized state to reduced state. Since those PPy(PAA) samples were doped with large immobile anions, these counterions could not be released from the PPy surface or matrix, which means the amount of immobilized BSA is approximately fixed. Hence, we could speculate that the intensity value changes seen in the PPy(PAA)-BSA cases were not due to the loss of the quantity of BSA but the change in BSA presentation, because the as-fabricated state has the most β sheet layers, which leads to the fewer active sites of BSA that may interact with the external environment. The oxidized state has the second highest content of β sheets, which is less compact than the as-fabricated state but still a compact structure, thus there are a little bit more active sites than in the as-fabricated state. However, the BSA in the reduced state comprises α-helices mostly, which are loose and result in most active sites presented to the external environment. Therefore, the fluorescence of PAA series samples changed based on the presentation of BSA, *i.e.*, the more "erected" the presentation of the BSA, the more the number of active sites of BSA exposed to the environment, the higher the fluorescence intensity. Hence, the presentation of BSA in different redox states could be confirmed, *i.e.*, the BSA in the as-fabricated state is "collapsed", in the oxidized state is "less collapsed" and in the reduced state is "erected".

Based on all the characterization results of CV, surface properties, surface morphology, IRAS and fluorescence images, we can postulate that the BSA presentation switches from "collapsed" in the as-fabricated state to "less collapsed" in the oxidized state and "erected" on the reduced PPy surfaces, as illustrated in Fig. 1a and 7. For future work, in line with the switching mechanism of BSA, we speculate that if the SCFs were immobilized on the PPy surface, when the electroactive PPy surface is reduced, the SCFs would also show an "erected" state and be available for interaction with the HSCs. In contrast, when the SCFs collapse on the PPy surface in the as-fabricated state, this could limit the recognition by the receptors of the HSCs. The "less collapsed" presentation of SCFs in the oxidized state would have a little bit more recognition possibility for the receptors than the as-fabricated state. Based on this principle, the diverse changeable biological environment could be mimicked by controlling the redox PPy surface in future studies. Fig. 10 illustrates that the reversible redox reactions result in reversible redox states and stable switching of the water contact angle, indicating the reversible switching of the BSA representation.

3.3 Cell viability

To investigate the possibility of surface toxicity, $CD45^+$ c-KIT^+ hematopoietic cells were incubated for 48 hours in a 48-well plate with each well bottom either containing no surface, *i.e.* blank (control) or an OXA, SUCA, PAA1200, PAA2100, or PAA8000 doped PPy-BSA surface. Flow cytometry analysis of incubated cells was performed; the representative gating scheme for control samples can be viewed in Fig. 11A and of cells incubated on the doped PPy-BSA surfaces in Fig. 11B. CD45 expression was used to distinguish cells from debris. Cell viability was normalized against the control and no significant difference in cell survival could be observed between the control and the different doped PPy-BSA surfaces, OXA (p = 0.35), PAA1200 (p = 0.99), PAA2100 (p = 0.82), PAA8000 (p = 0.76), and SUCA (p = 0.55) (Fig. 11C). We also investigated the total $CD45^+$ cell numbers to ensure that the doped PPy-BSA surfaces did not reduce the proliferative ability. OXA (p = 0.89), PAA1200 (p = 0.68), and PAA8000 (p = 0.72) displayed no significant difference in $CD45^+$ cell count compared to the control, while PAA2100 (p = 0.05), and SUCA (p = 0.05) displayed a significant increase of $CD45^+$ cells compared to the control (Fig. 11D). These results clearly show that the developed PPy-BSA surfaces did not negatively alter cell viability or cell proliferation compared to the control.

4 Conclusion

This paper describes a proof-of-concept of a bioelectroactive surface to modulate cellular behavior in a complex microenvironment. We report how such bioelectroactive surfaces comprising PPy with COOH groups, PPy doped with dicarboxylic acids with different lengths of the carbon chains, and PPy doped with polycarboxylic acids of different molecular weights were used for the immobilization of BSA to simulate the covalent bonding of SCF.[1] The results demonstrate that the ability of the different dopants to immobilize BSA on the PPy surface is different. The PPy(PAA) series comprises the most suitable samples for the immobilization of BSA on the surface. Next, a study of the presentation of immobilized BSA on the PPy surface in different redox states was carried out. The results demonstrate that the presentation of immobilized BSA could be altered by applying a redox potential to the surface and depended on the dopant used. In addition, the redox switching also indicates different presentations of BSA on different PPy surfaces. For unsubstituted PPy-BSA samples, BSA showed a "less collapsed" presentation in the oxidized state, whereas BSA showed an "erected" presentation on PPy in the reduced state. Since this study contrasts different types of PPy surfaces prepared with various carboxylic acid dopants, it provides a good starting point for our future immobilization of SCFs for HSC studies. Cell viability studies using hematopoietic cells showed that the developed PPy-BSA surfaces did not negatively alter cell viability or cell proliferation compared to the control.

The concept of dynamically changing the presentation of immobilized biomolecules upon redox activation gives a way to dynamically adjust cell proliferation. Since different presentations of the biomolecules expose the active sites to a different extent, various states of SCF (*e.g.,* growth, proliferation, and differentiation-inducing) could possibly be induced by the redox state of the surfaces. However, in addition to the artificial microenvironment as studied here, other relevant components, such as culture media and cytokines and growth factor composition, need to be addressed simultaneously.

Therefore, future research will also address studying the dynamic behavior of SCF under electrochemical control in complex biological microenvironments and long-term stability. The success of *in vitro* expansion of HSCs in the future would provide more therapeutic options for people with blood disorders. Therefore, the results of this and future studies may lead to positive effects on patient treatment. Moreover, we found that the PPyCOOH film electrodissolved when a reduced potential was applied. This finding could be used to develop surfaces that enable detaching cells from a surface, *i.e.*, electrodes.

Data availability

All data are available from the authors upon request.

Conflicts of interest

There are no conflicts to declare.

Acknowledgements

This study was supported by Linköping University and the China Scholarship Council (201808330454).

References

1 H. Sung, *et al.*, Global cancer statistics 2020: GLOBOCAN estimates of incidence and mortality worldwide for 36 cancers in 185 countries, *CA-Cancer J. Clin.*, 2021, **71**(3), 209–249.
2 M. Lyu, *et al.*, Comparison of autologous and allogeneic stem cell transplantation for patients with Philadelphia chromosome-positive acute lymphoblastic leukemia, *Hematology*, 2021, **26**(1), 65–74.
3 S. Almalki, Investigation of haematopoietic stem cell homing post-transplantation, using an in vitro model of the bone marrow/vasculature interface, in *Faculty of Health and Applied Sciences*, University of the West of England, 2021.
4 P. Tajer, *et al.*, Ex vivo expansion of hematopoietic stem cells for therapeutic purposes: lessons from development and the niche, *Cells*, 2019, **8**(2), 169.
5 X.-S. Jiang, *et al.*, Surface-immobilization of adhesion peptides on substrate for ex vivo expansion of cryopreserved umbilical cord blood CD34 + cells, *Biomaterials*, 2006, **27**(13), 2723–2732.
6 J. Baumgartner, J.-I. Jönsson and E. W. Jager, Switchable presentation of cytokines on electroactive polypyrrole surfaces for hematopoietic stem and progenitor cells, *J. Mater. Chem. B*, 2018, **6**(28), 4665–4675.
7 A. Herland, *et al.*, Electrochemical control of growth factor presentation to steer neural stem cell differentiation, *Angew. Chem., Int. Ed.*, 2011, **50**(52), 12529–12533.
8 R. Balint, N. J. Cassidy and S. H. Cartmell, Conductive polymers: Towards a smart biomaterial for tissue engineering, *Acta Biomater.*, 2014, **10**(6), 2341–2353.
9 C. Pitsalidis and R. Owens, Conducting polymer scaffold device as a tool to mimic and monitor 3D tissue microenvironment for use in organ-on-chip platforms, in *Organic and Hybrid Sensors and Bioelectronics XV*, SPIE, 2022.
10 J. A. Goding, *et al.*, Living Bioelectronics: Strategies for Developing an Effective Long–Term Implant with Functional Neural Connections, *Adv. Funct. Mater.*, 2018, **28**(12), 1702969.
11 N. Gomez and C. E. Schmidt, Nerve growth factor–immobilized polypyrrole: Bioactive electrically conducting polymer for enhanced neurite extension, *J. Biomed. Mater. Res., Part A*, 2007, **81**(1), 135–149.
12 S. Wang, *et al.*, The effect of physical cues of biomaterial scaffolds on stem cell behavior, *Adv. Healthcare Mater.*, 2021, **10**(3), 2001244.
13 N. K. Guimard, N. Gomez and C. E. Schmidt, Conducting polymers in biomedical engineering, *Prog. Polym. Sci.*, 2007, **32**(8–9), 876–921.
14 J. Isaksson, *et al.*, A Solid–State Organic Electronic Wettability Switch, *Adv. Mater.*, 2004, **16**(4), 316–320.
15 J. Liao, *et al.*, Reversibly controlling preferential protein adsorption on bone implants by using an applied weak potential as a switch, *Angew. Chem.*, 2014, **126**(48), 13284–13288.
16 Y. Wei, *et al.*, Directing stem cell differentiation via electrochemical reversible switching between nanotubes and nanotips of polypyrrole array, *ACS Nano*, 2017, **11**(6), 5915–5924.
17 D. Melling, J. G. Martinez and E. W. Jager, Conjugated polymer actuators and devices: progress and opportunities, *Adv. Mater.*, 2019, **31**(22), 1808210.
18 L. Yang, *et al.*, Electrochemically-driven actuators: from materials to mechanisms and from performance to applications, *Chem. Soc. Rev.*, 2024, **53**(11), 5956–6010.
19 A. Hameed, *et al.*, Insulin-like growth factor-1 (IGF-1) poly (lactic-co-glycolic acid)(PLGA) microparticles–development, characterisation, and in vitro assessment of bioactivity for cardiac applications, *J. Microencapsulation*, 2019, **36**(3), 267–277.
20 J. Ziegler, *et al.*, Biological activity of recombinant human growth factors released from biocompatible bone implants, *J. Biomed. Mater. Res.*, 2008, **86**(1), 89–97.
21 R. Budiraharjo, K. G. Neoh and E.-T. Kang, Enhancing bioactivity of chitosan film for osteogenesis and wound healing by covalent immobilization of BMP-2 or FGF-2, *J. Biomater. Sci., Polym. Ed.*, 2013, **24**(6), 645–662.
22 V. Midy, *et al.*, Basic fibroblast growth factor adsorption and release properties of calcium phosphate, *J. Biomed. Mater. Res.*, 1998, **41**(3), 405–411.
23 Z. Wang, *et al.*, Novel biomaterial strategies for controlled growth factor delivery for biomedical applications, *NPG Asia Mater.*, 2017, **9**(10), e435–e435.

24 E. S. Place, *et al.*, Latent TGF–β Hydrogels for Cartilage Tissue Engineering, *Adv. Healthcare Mater.*, 2012, **1**(4), 480–484.
25 Y.-P. Li, *et al.*, PEGylated PLGA nanoparticles as protein carriers: synthesis, preparation and biodistribution in rats, *J. Controlled Release*, 2001, **71**(2), 203–211.
26 A. Erfani, *et al.*, Effect of zwitterionic betaine surfactant on interfacial behavior of bovine serum albumin (BSA), *J. Mol. Liq.*, 2020, **318**, 114067.
27 W. Gospodarczyk and M. Kozak, Interaction of two imidazolium gemini surfactants with two model proteins BSA and HEWL, *Colloid Polym. Sci.*, 2015, **293**(10), 2855–2866.
28 M. Hayat, S. A. R. Bukhari and M. Irfan, Electrospinning of bovine serum albumin-based nano-fibers: From synthesis to medical prospects; Challenges and future directions, *Biotechnol. J.*, 2023, **18**(12), 2300279.
29 J. J. Babcock and L. Brancaleon, Bovine serum albumin oligomers in the E- and B-forms at low protein concentration and ionic strength, *Int. J. Biol. Macromol.*, 2013, **53**, 42–53.
30 Y. L. Jeyachandran, *et al.*, Quantitative and qualitative evaluation of adsorption/desorption of bovine serum albumin on hydrophilic and hydrophobic surfaces, *Langmuir*, 2009, **25**(19), 11614–11620.
31 V. Militello, *et al.*, Thermal aggregation of proteins in the presence of metal ions, in *Biophysical Inquiry into Protein Aggregation and Amyloid Diseases*, eds. P. L. San Biagio and D. Bulone, Transworld Research Network, Trivandrum, Kerala, India, 2008, pp. 181–232.
32 K. Murayama and M. Tomida, Heat-Induced Secondary Structure and Conformation Change of Bovine Serum Albumin Investigated by Fourier Transform Infrared Spectroscopy, *Biochemistry*, 2004, **43**(36), 11526–11532.
33 L. Meng, A. Turner and W. C. Mak, Modulating electrode kinetics for discrimination of dopamine by a PEDOT: COOH interface doped with negatively charged tricarboxylate, *ACS Appl. Mater. Interfaces*, 2019, **11**(37), 34497–34506.
34 A. Retnakumari, *et al.*, Molecular-receptor-specific, non-toxic, near-infrared-emitting Au cluster-protein nanoconjugates for targeted cancer imaging, *Nanotechnology*, 2010, **21**(5), 055103.
35 M. J. Jafari, *et al.*, Force-Induced Structural Changes in Spider Silk Fibers Introduced by ATR-FTIR Spectroscopy, *ACS Appl. Polym. Mater.*, 2023, **5**(11), 9433–9444.
36 C. Guo, *et al.*, Spectroscopic study of conformation changes of bovine serum albumin in aqueous environment, *Chin. Chem. Lett.*, 2019, **30**(6), 1302–1306.
37 R. I. Litvinov, *et al.*, The α-Helix to β-Sheet Transition in Stretched and Compressed Hydrated Fibrin Clots, *Biophys. J.*, 2012, **103**(5), 1020–1027.
38 A. Fadlelmoula, *et al.*, Fourier Transform Infrared (FTIR) Spectroscopy to Analyse Human Blood over the Last 20 Years: A Review towards Lab-on-a-Chip Devices, *Micromachines*, 2022, **13**(2), 187.
39 D. Tretiakova, *et al.*, Spectroscopy Study of Albumin Interaction with Negatively Charged Liposome Membranes: Mutual Structural Effects of the Protein and the Bilayers, *Membranes*, 2022, **12**(11), 1031.
40 Z. Cheng, *et al.*, A facile bacterial assisted electrochemical self-assembly of polypyrrole micro-pillars: towards underwater low adhesive superoleophobicity, *Nanoscale*, 2014, **6**(1), 190–194.
41 H. B. Fredj, *et al.*, Labeled magnetic nanoparticles assembly on polypyrrole film for biosensor applications, *Talanta*, 2008, **75**(3), 740–747.
42 S. Y. Lee, *et al.*, Covalent Surface Functionalization of Bovine Serum Albumin to Magnesium Surface to Provide Robust Corrosion Inhibition and Enhance In Vitro Osteo-Inductivity, *Polymers*, 2020, **12**(2), 439.
43 T. Silk, *et al.*, AFM studies of polypyrrole film surface morphology I. The influence of film thickness and dopant nature, *Synth. Met.*, 1998, **93**(1), 59–64.
44 I. M. Minisy, *et al.*, Methyl red dye in the tuning of polypyrrole conductivity, *Polymer*, 2020, **207**, 122854.
45 P. Jayamurgan, *et al.*, The effect of dopant on structural, thermal and morphological properties of DBSA-doped polypyrrole, *Iran. Polym. J.*, 2013, **22**(3), 219–225.
46 A. Gelmi, M. J. Higgins and G. G. Wallace, Physical surface and electromechanical properties of doped polypyrrole biomaterials, *Biomaterials*, 2010, **31**(8), 1974–1983.
47 A. Chanachev, *et al.*, Study of protein modified gold nanoparticles in bulk phase and at air/water interface, *Chemistry*, 2015, **24**(6), 863.
48 L.-C. Xu and B. E. Logan, Interaction forces measured using AFM between colloids and surfaces coated with both dextran and protein, *Langmuir*, 2006, **22**(10), 4720–4727.
49 P. M. George, *et al.*, Electrical preconditioning of stem cells with a conductive polymer scaffold enhances stroke recovery, *Biomaterials*, 2017, **142**, 31–40.
50 D. Xu, *et al.*, Tailorable hierarchical structures of biomimetic hydroxyapatite micro/nano particles promoting endocytosis and osteogenic differentiation of stem cells, *Biomater. Sci.*, 2020, **8**(12), 3286–3300.
51 T. F. Otero, Biomimetic conducting polymers: synthesis, materials, properties, functions, and devices, *Polym. Rev.*, 2013, **53**(3), 311–351.
52 J. Carrasco, *et al.*, Anodic electrosynthesis and cathodic electrodissolution of poly (2, 5-di-(2-thienyl) pyrrole). A new way of processibility, *Synth. Met.*, 1993, **61**(3), 253–258.
53 K. M. Persson, *et al.*, Electronic control of cell detachment using a self-doped conducting polymer, *Adv. Mater.*, 2011, **23**(38), 4403–4408.
54 D. Melling, S. Wilson and E. W. Jager, The effect of film thickness on polypyrrole actuation assessed using novel non-contact strain measurements, *Smart Mater. Struct.*, 2013, **22**(10), 104021.
55 K. Kopeć, *et al.*, Comparison of α-helix and β-sheet structure adaptation to a quantum dot geometry: Toward the identification of an optimal motif for a protein nanoparticle cover, *ACS Omega*, 2019, **4**(8), 13086–13099.
56 E. P. DeBenedictis and S. Keten, Mechanical unfolding of alpha-and beta-helical protein motifs, *Soft Matter*, 2019, **15**(6), 1243–1252.